Electronic Supplementary Information (ESI) for

The radicals of quercetin-derived antioxidants in Triton X-100 micelles

Tim Kohlmann and Martin Goez[*]

Contents

[*]Tim Kohlmann, Prof. Dr. Martin Goez,
Martin-Luther-Universität Halle-Wittenberg, Institut für Chemie, Kurt-Mothes-Str. 2, D-06120 Halle (Saale), Germany.
E-mail: martin.goez@chemie.uni-halle.de

1 Experimental Details

All chemicals (quercetin, $>$ 96 %, Sigma-Aldrich; 3-O-methylquercetin, $\geq$ 97 %, Sigma-Aldrich; rutin, 95.7 %, Sigma-Aldrich; narcisssin, 99 %, Phytolab; azaleatin, 97 %, abcr; rhamnetin, 99.5 %, Sigma-Aldrich; rhamnazin, $\geq$ 99 %, Sigma-Aldrich; isorhamnetin, $\geq$ 95 %, Sigma-Aldrich; tamarixetin, 99 %, abcr; rhamnetin-3-galactoside, ChemFaces, $>$ 98 %; Triton X-100, Sigma-Aldrich, BioXtra) were used as received.

Solutions were always freshly prepared with ultrapure Millipore Milli-Q water (specific resistance, 18.2 MΩ cm^{-1}). Prior to use, they were deoxygenated for at least 30 minutes with Ar 5.0 or — when $e_{aq}^{\bullet-}$ had to be scavenged — with N_2O 5.0, both from AirLiquide. For the steady-state absorption measurements, sealed cuvettes were employed; and for the flow-through laser flash photolysis experiments, a stream of the respective inert gas was continuously maintained above the solution in the stock vessel.

Unless otherwise stated, the substrate concentration was always 10 μM and the surfactant concentration 50 mM. The desired pH values were adjusted under pH meter control by the addition of HCl or NaOH, with volume changes rendered negligible by adding the concentrated acid or base with microliter syringes.

Steady-state absorption measurements were carried out with a Shimadzu UV-1800 spectrophotometer. For the laser flash studies we used a home-made setup described in detail elsewhere.[1] Its following features are of particular importance for the present work. Photolysis is performed with a frequency-tripled (355 nm) pulsed Nd:YAG laser (Continuum Surelite-III; pulse width, 5 ns). The laser beam is collimated such that it homogeneously fills a 46 μL volume (height, 2.9 mm; width and depth, 4 mm each) of a suprasil cell with intensities of up to 500 mJ cm^{-2}. Up to 40 % of the substrates can thus be photoionized with a single flash; and, on account of the optically thin solutions, calibrated absorption spectra and kinetics of the transients can be reliably recorded with a time resolution down to 1 ns. A syringe-driven flow-through system ensures that each acquisition takes place on fresh solution.

Specific experimental procedures are explained in the pertaining sections, and details of the quantum-mechanical calculations are given in ESI-4.

2 Ground-State Properties

2.1 Micellar Complexation

Moroi's formal-kinetic treatment of solubilization,[2] which properly takes into account the Poisson distribution of the micellar occupants, shows that the equilibrium between the guest molecules in the aqueous bulk and in the micelles, Q_{aq} and Q_{mic}, is simply describable by Supplementary Equation S1, i.e., as if the surfactant $Surf_m$ in its aggregated state were an

ordinary chemical reactant,

$$\mathrm{Q_{aq}} + \mathrm{Surf_m} \quad \overset{K}{\rightleftharpoons} \quad \mathrm{Q_{mic}} \tag{S1}$$

except that its concentration does not change in the process.

The weight-in concentration $[\mathrm{Q_t}]$ obviously equals the sum of $\left[\mathrm{Q_{aq}}\right]$ and $[\mathrm{Q_{mic}}]$, and the concentration of $\mathrm{Surf_m}$ is connected with its weight-in concentration $[\mathrm{Surf_t}]$ through Supplementary Equation S2,

$$[\mathrm{Surf_m}] \quad = \quad \frac{[\mathrm{Surf_t}] - \mathrm{cmc}}{N_{\mathrm{agg}}} \tag{S2}$$

with the surfactant-specific critical micelle concentration cmc and aggregation number N_{agg}.

Rearranging the mass-action law for the chemical equilibrium of Supplementary Equation S1 and inserting the described relationships one arrives at Supplementary Equations S3a and S3b for the relative concentrations of Q in the different surroundings,

$$\frac{\left[\mathrm{Q_{aq}}\right]}{[\mathrm{Q_t}]} \quad = \quad \frac{1}{1 + \left(K/N_{\mathrm{agg}}\right)\left([\mathrm{Surf_t}] - \mathrm{cmc}\right)} \quad = \quad \frac{1}{1 + K'\left([\mathrm{Surf_t}] - \mathrm{cmc}\right)} \tag{S3a}$$

$$\frac{[\mathrm{Q_{mic}}]}{[\mathrm{Q_t}]} \quad = \quad \frac{\left(K/N_{\mathrm{agg}}\right)\left([\mathrm{Surf_t}] - \mathrm{cmc}\right)}{1 + \left(K/N_{\mathrm{agg}}\right)\left([\mathrm{Surf_t}] - \mathrm{cmc}\right)} \quad = \quad \frac{K'\left([\mathrm{Surf_t}] - \mathrm{cmc}\right)}{1 + K'\left([\mathrm{Surf_t}] - \mathrm{cmc}\right)} \tag{S3b}$$

As is evident from these equations, no separation of K and N_{agg} ist possible, and both combine into a single constant K'.

With the extinction coefficients $\varepsilon_{\mathrm{aq}}$ and $\varepsilon_{\mathrm{mic}}$ for Q in the respective (pseudo)phase, the observed extinction coefficient ε follows from Supplementary Equation S4,

$$\varepsilon \quad = \quad \frac{\varepsilon_{\mathrm{aq}} + \varepsilon_{\mathrm{mic}} K'\left([\mathrm{Surf_t}] - \mathrm{cmc}\right)}{1 + K'\left([\mathrm{Surf_t}] - \mathrm{cmc}\right)} \tag{S4}$$

The quantity $\varepsilon_{\mathrm{aq}}$ can be precisely measured in the absence of the surfactant; cmc can be determined by independent experiments; and $\varepsilon_{\mathrm{mic}}$ will usually be accessible in the limit of high $[\mathrm{Surf_t}]$. This leaves K' as the only freely adjustable parameter.

We stress that the only approximation involved in the derivation of Supplementary Equation S4 concerns Supplementary Equation S2: for charged surfactants such as SDS, the relationship between $[\mathrm{Surf_m}]$ and $[\mathrm{Surf_t}]$ depends in a more complex way on the concentration of the common counterion.[3]

Transforming Supplementary Equation S4 to give a Benesi–Hildebrand-type equation would be straightforward,

$$\frac{1}{\varepsilon - \varepsilon_{\mathrm{aq}}} \quad = \quad \frac{1}{\varepsilon_{\mathrm{mic}} - \varepsilon_{\mathrm{aq}}} \quad + \quad \frac{1}{K'\left(\varepsilon_{\mathrm{mic}} - \varepsilon_{\mathrm{aq}}\right)} \times \frac{1}{[\mathrm{Surf_t}] - \mathrm{cmc}} \tag{S5}$$

but the nonlinear fit of Supplementary Equation S4 possesses the advantage over the linear fit of Supplementary Equation S5 that it does not distort the statistical weights of the individual data points.

Supplementary Figures 1a and 1b display the results of complexation experiments by Triton TX–100 for the parent compound quercetin and its more hydrophilic derivative rutin. A pH of 4.5 ensured that each substrate was present practically exclusively in its protonated form. The micellar medium causes a bathochromic shift of the longest-wavelength absorption band by about 10 nm compared to aqueous medium (quercetin, 367 nm $\rightarrow$ 376 nm; rutin, 351 nm $\rightarrow$ 361 nm), which is accompanied by a small rise of the maximum height (quercetin, 13 %; rutin, 7 %). To improve the sensitivity by increasing the changes, we took slices through the spectra at about half-height of the respective band, to the right of its maximum (quercetin, 390 nm; rutin, 380 nm). The cmc of TX–100 is 0.24 mM.[4] As expected, the complexation constant K' is found to be much larger for quercetin than for rutin (1.8×10^4 M^{-1} *vs* 3.1×10^2 M^{-1}). Inserting these results into Supplementary Equation S3a reveals that less than 6 % of rutin reside in the aqueous phase at the surfactant concentration used in all other experiments of this work (50 mM); that fraction decreases to 0.1 % for quercetin, and must be utterly negligible in the case of the even more hydrophobic methyl ethers.

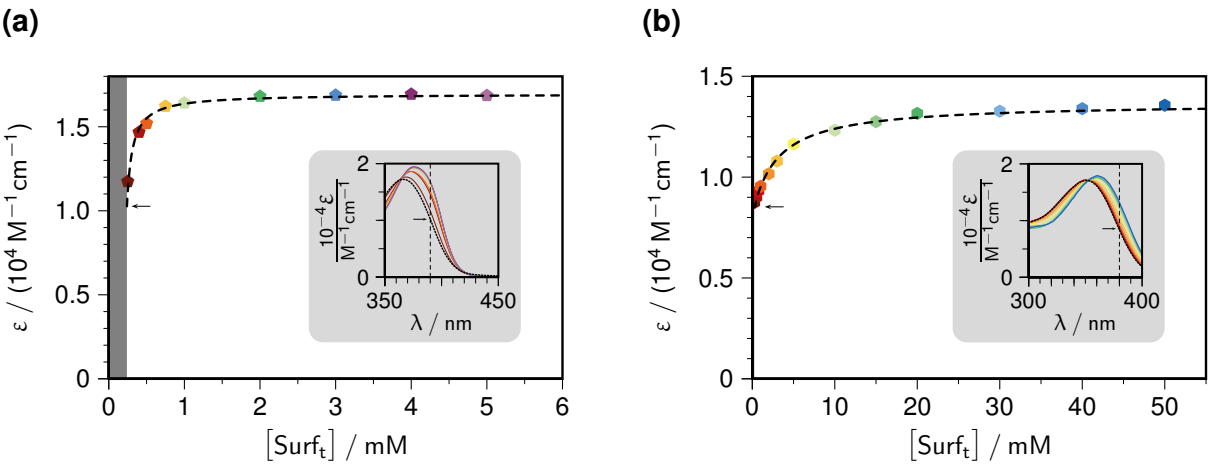

Supplementary Figure 1: Complexation of 10 μM quercetin (a) or rutin (b) by Triton TX–100 micelles at pH 4.5. Insets, spectra at different surfactant weight-in concentrations [$Surf_t$]; main plots, extinction coefficients ε as functions of [$Surf_t$] at the wavelength indicated by the vertical dashed line in the corresponding inset. Identical color code for [$Surf_t$] between each main plot and its inset; spectra in water displayed as dotted curves; pertaining ε at the observation wavelength indicated by horizontal arrows; cmc of TX–100 (0.24 mM) shown as an exclusion zone by a rectangle filled with gray in the main plot of graph (a), and invisible in the case of (b). Dashed curves in the main plots, fits of Supplementary Equation S4; best-fit values of K', 1.8×10^4 M^{-1} (a) and 3.1×10^2 M^{-1} (b). For further explanation, see the text.

2.2 Ground-State pKa

Supplementary Figures 2–10 display pH-dependent absorption spectra, which were recorded to determine the first pK_a of our substrates. Well-defined isosbestic points are only found for rutin $Q\overline{3_g}$ and azaleatin $Q\overline{5}$; their lack for the other compounds indicates closely-lying pK_a values of their other deprotonation sites, such that their first pK_a is an apparent quantity.

However, knowledge of that apparent pK_a provides a pH window within which the generation of the radicals starts out from the fully protonated substrates (pH $\leq$ 6.5 in most cases; pH $\leq$ 6.2 with rutin and 3-O-methylquercetin,$Q\overline{3_g}$ and $Q\overline{3}$).

For better comparison with the titration curves, the relative photoionization yields have been included in Supplementary Figures 2b, 3b, 4b, and 5b. These will be discussed in ESI-3.1.

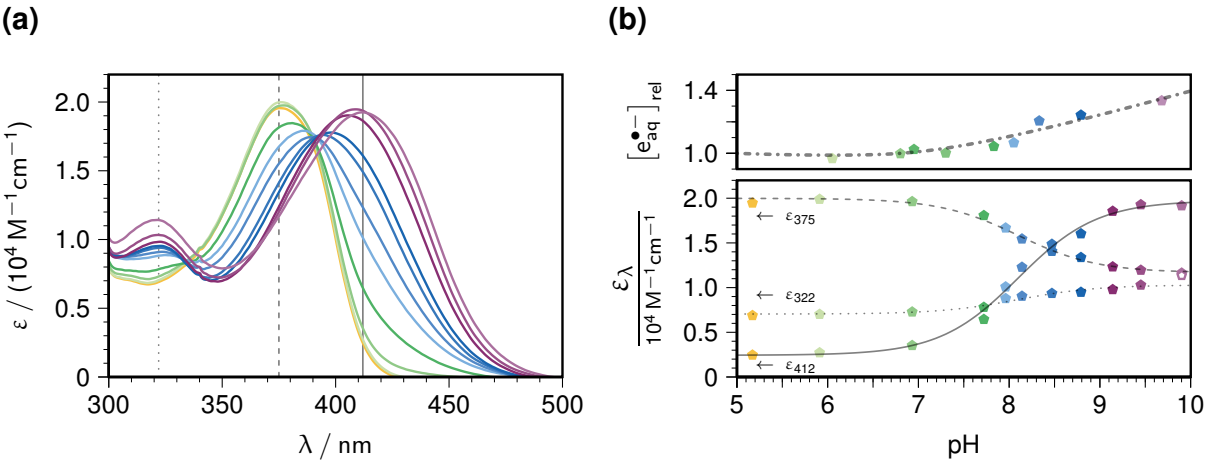

Supplementary Figure 2: Deprotonation and photoionization of quercetin Q. Graph (a), pH dependent absorption spectra. Graph (b), lower part: determination of the first pK_a by taking slices through the spectra at 412 nm (solid), 375 nm (dashed), and 322 nm (dotted); global best-fit pK_a, 8.10, highest pH (open data points) excluded. Graph (b), upper part: pH-dependent relative photoionization yields; fit function without physical significance. Concentrations, 10 μM of substrate in 50 mM aqueous Triton TX-100 micellar solution; identical color code for the pH between the graphs. For further explanation, see the text.

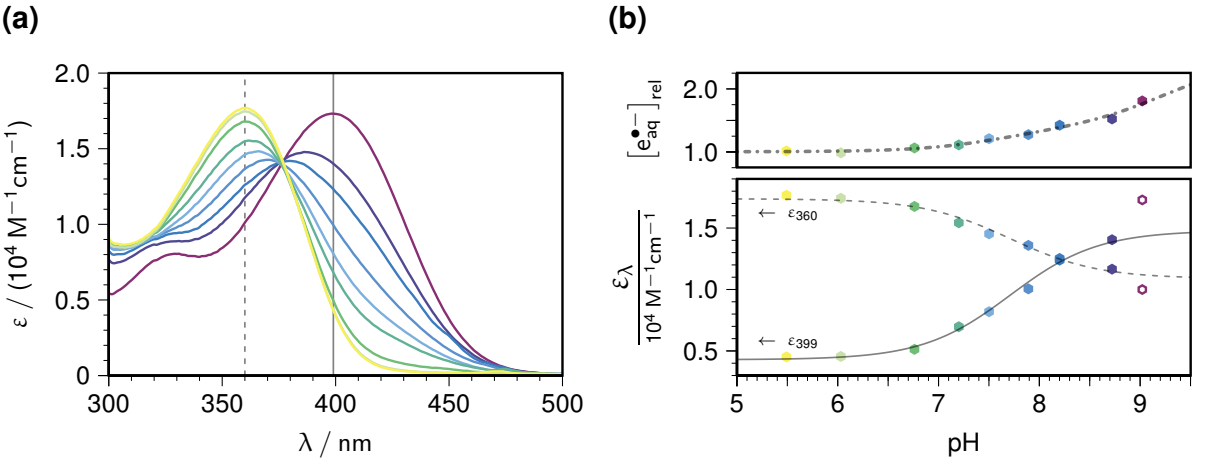

Supplementary Figure 3: Deprotonation and photoionization of rutin $Q\overline{3_g}$. Graph (a), pH dependent absorption spectra. Graph (b), lower part: determination of the first pK_a by taking slices through the spectra at 399 nm (solid) and 360 nm (dashed); global best-fit pK_a,7.71, highest pH (open data points) excluded. Graph (b), upper part: pH-dependent relative photoionization yields; fit function without physical significance. Concentrations, 10 μM of substrate in 50 mM aqueous Triton TX-100 micellar solution; identical color code for the pH between the graphs. For further explanation, see the text.

At pH 3 and 6.5, the ground-state spectra of 3-O-methylquercetin Q$\overline{3}$ are identical. Given that its transient spectra are also identical to those of rutin Q$\overline{3_g}$ at both pH values and in view of the relatively high price of Q$\overline{3}$, we did not determine its pK_a. It should be very similar to that of Q$\overline{3_g}$ on account of the identical substitution pattern.

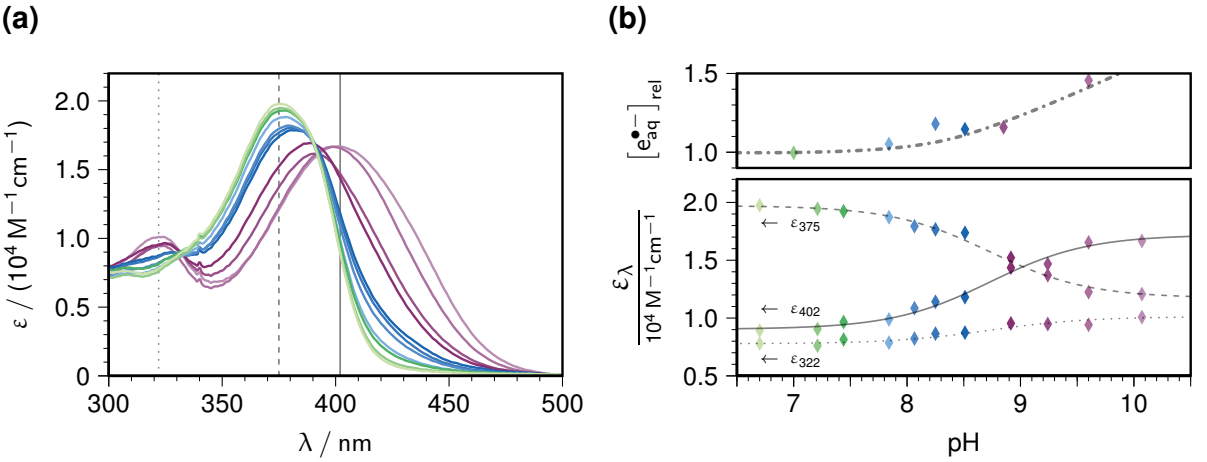

Supplementary Figure 4: Deprotonation and photoionization of isorhamnetin Q$\overline{3'}$. Graph (a), pH dependent absorption spectra. Graph (b), lower part: determination of the first pK_a by taking slices through the spectra at 402 nm (solid), 375 nm (dashed), and 322 nm (dotted); global best-fit pK_a, 8.73. Graph (b), upper part: pH-dependent relative photoionization yields; fit function without physical significance. Concentrations, 10 μM of substrate in 50 mM aqueous Triton TX-100 micellar solution; identical color code for the pH between the graphs. For further explanation, see the text.

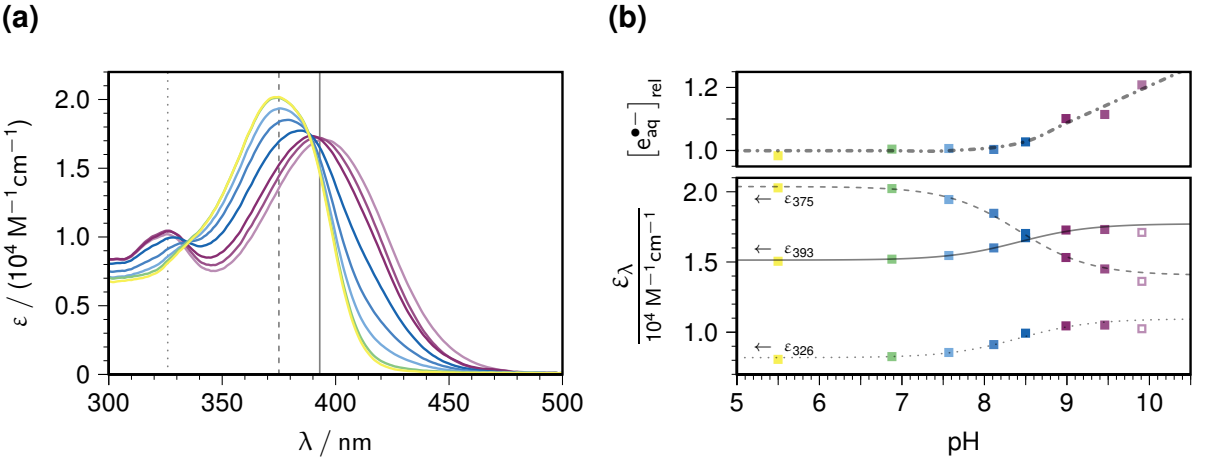

Supplementary Figure 5: Deprotonation and photoionization of tamarixetin Q$\overline{4'}$. Graph (a), pH dependent absorption spectra. Graph (b), lower part: determination of the first pK_a by taking slices through the spectra at 393 nm (solid), 375 nm (dashed), and 326 nm (dotted); global best-fit pK_a, 8.42, highest pH (open data points) excluded. Graph (b), upper part: pH-dependent relative photoionization yields; fit function without physical significance. Concentrations, 10 μM of substrate in 50 mM aqueous Triton TX-100 micellar solution; identical color code for the pH between the graphs. For further explanation, see the text.

Because of availability and price, no pH-dependent photoionization yields were measured for azaleatin Q$\overline{5}$, rhamnetin Q$\overline{7}$, rhamnazin Q$\overline{3'7}$, narcissin Q$\overline{3_g 3'}$, and rhamnetin-3-galactoside Q$\overline{3_g 7}$. The pK_a values of these substrates are among the highest of all the derivatives, at least 8.6, and a participation of their monodeprotonated forms in the photoionizations is extremely unlikely at a pH two units below the pK_a.

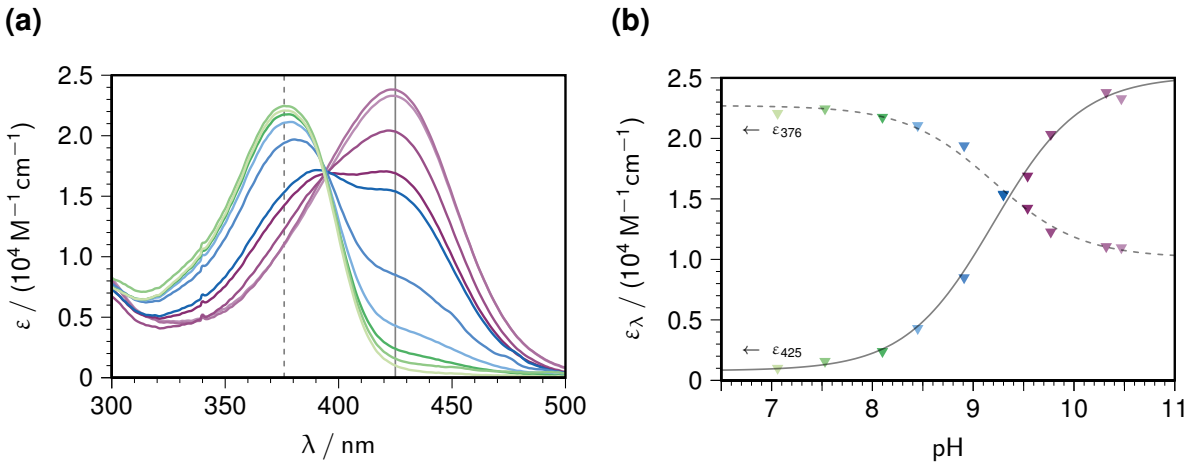

Supplementary Figure 6: Deprotonation of azaleatin Q$\overline{5}$. Graph (a), pH dependent absorption spectra. Graph (b), determination of the first pK_a by taking slices through the spectra at 425 nm (solid) and 376 nm (dashed); global best-fit pK_a, 9.20. Concentrations, 10 μM of substrate in 50 mM aqueous Triton TX-100 micellar solution; identical color code for the pH between the graphs. For further explanation, see the text.

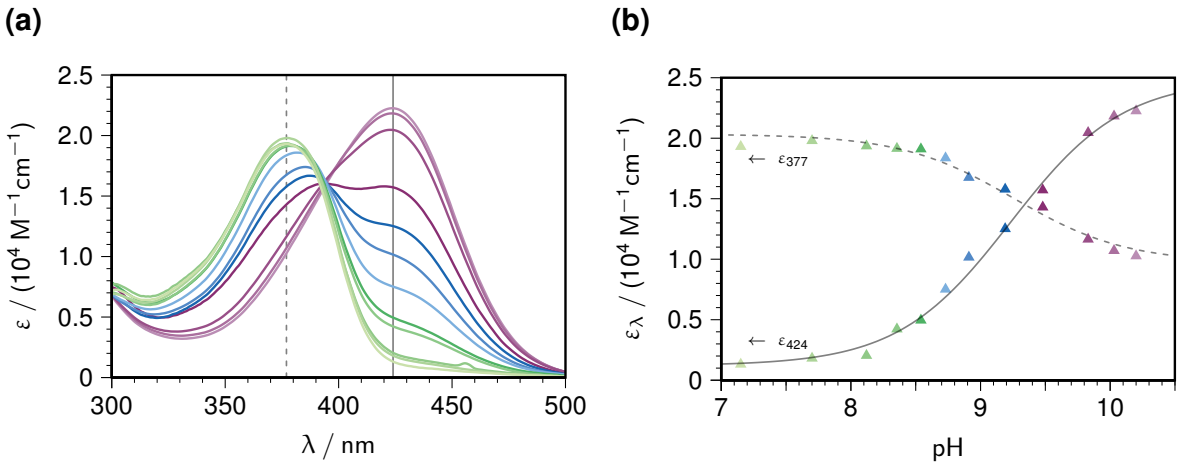

Supplementary Figure 7: Deprotonation of rhamnetin Q$\overline{7}$. Graph (a), pH dependent absorption spectra. Graph (b), determination of the first pK_a by taking slices through the spectra at 424 nm (solid) and 377 nm (dashed); global best-fit pK_a, 9.23. Concentrations, 10 μM of substrate in 50 mM aqueous Triton TX-100 micellar solution; identical color code for the pH between the graphs. For further explanation, see the text.

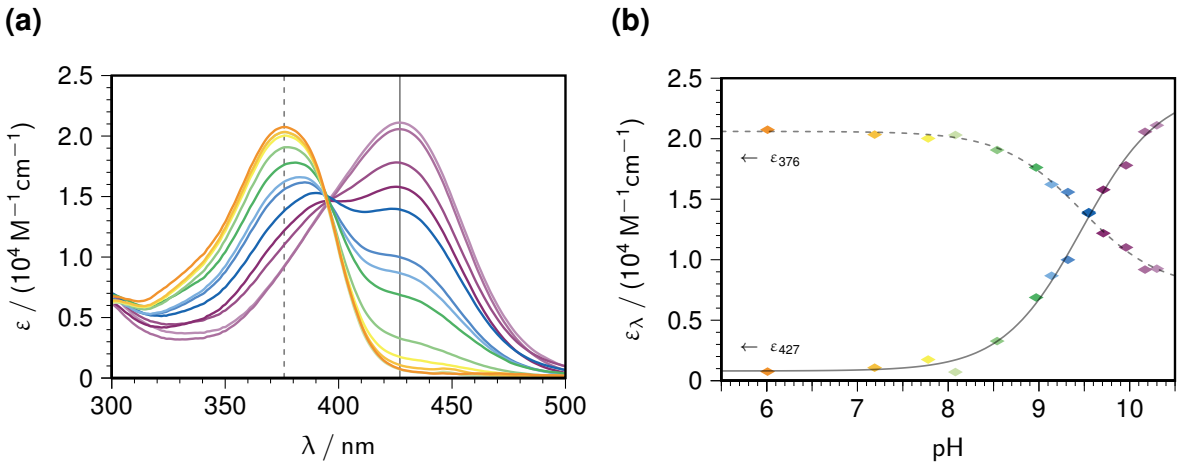

Supplementary Figure 8: Deprotonation of rhamnazin Q$\overline{3'7}$. Graph (a), pH dependent absorption spectra. Graph (b), determination of the first pK_a by taking slices through the spectra at 427 nm (solid) and 376 nm (dashed); global best-fit pK_a, 9.47. Concentrations, 11.5 μM of substrate in 50 mM aqueous Triton TX-100 micellar solution; identical color code for the pH between the graphs. For further explanation, see the text.

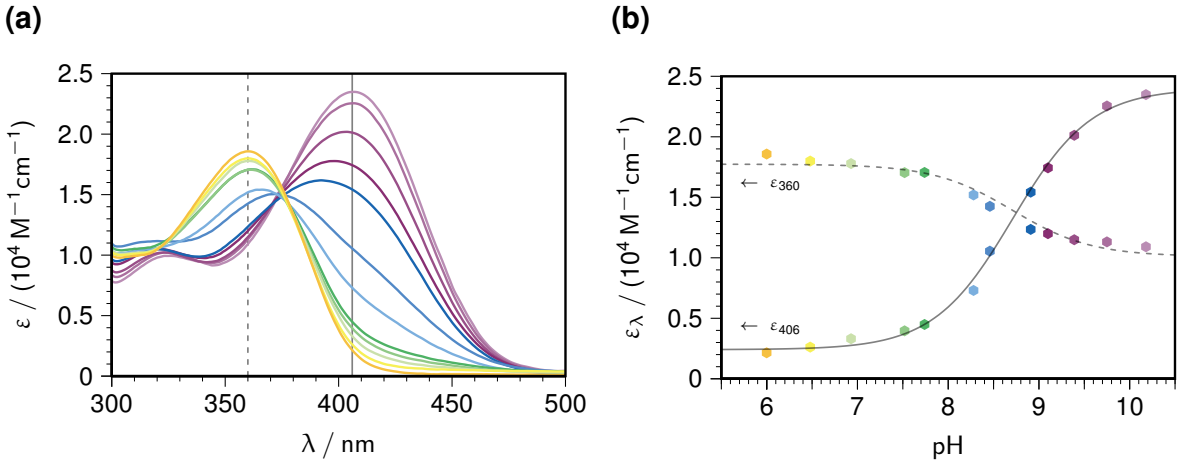

Supplementary Figure 9: Deprotonation of narcissin Q$\overline{3_g3'}$. Graph (a), pH dependent absorption spectra. Graph (b), determination of the first pK_a by taking slices through the spectra at 406 nm (solid) and 360 nm (dashed); global best-fit pK_a, 8.71. Concentrations, 10 μM of substrate in 50 mM aqueous Triton TX-100 micellar solution; identical color code for the pH between the graphs. For further explanation, see the text.

Points at pH values well above the pK_a have been excluded from the preceding fits when the next deprotonation step clearly takes over (Supplementary Figures 2, 3, and 5).

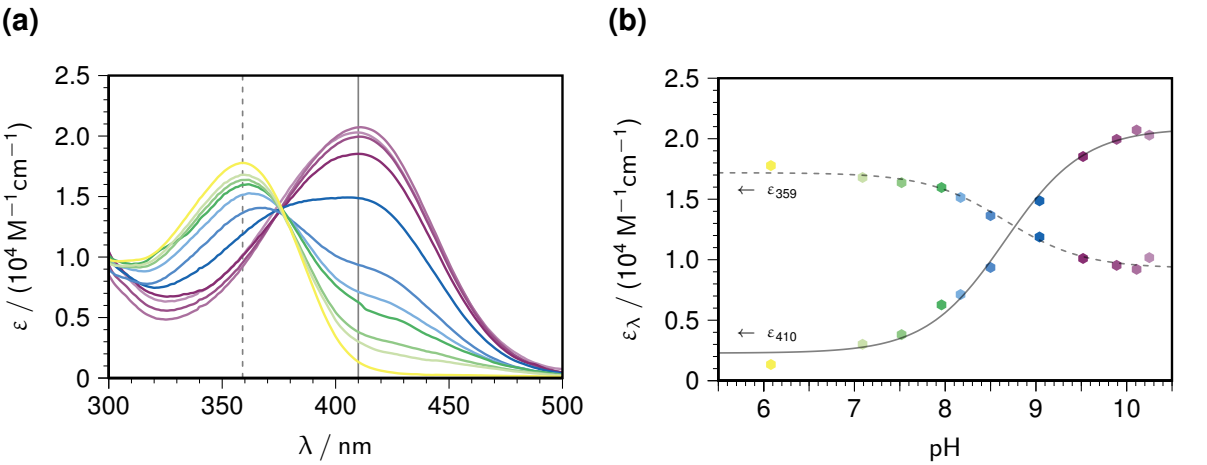

Supplementary Figure 10: Deprotonation of rhamnetin-3-galactoside Q$\overline{3_g7}$. Graph (a), pH dependent absorption spectra. Graph (b), determination of the first pK_a by taking slices through the spectra at 410 nm (solid) and 359 nm (dashed); global best-fit pK_a, 8.66. Concentrations, 10 μM of substrate in 50 mM aqueous Triton TX-100 micellar solution; identical color code for the pH between the graphs. For further explanation, see the text.

Supplementary Figure 11 collects the ground-state absorption spectra of all the investigated compounds in their protonated forms. Included have been the pair of analogues rutin Q$\overline{3_g}$ and 3-O-methylquercetin Q$\overline{3}$, as well as the disubstituted derivatives rhamnazin Q$\overline{3'7}$, narcissin Q$\overline{3_g3'}$, and rhamnetin-3-galactoside Q$\overline{3_g7}$. As is evident, alkyl substitution (etherification) at the oxygens in positions 3′, 4′, 5, and 7 has only a negligible influence on the spectra, whereas in position 3 it effects a hypsochromic shift by some 20 nm.

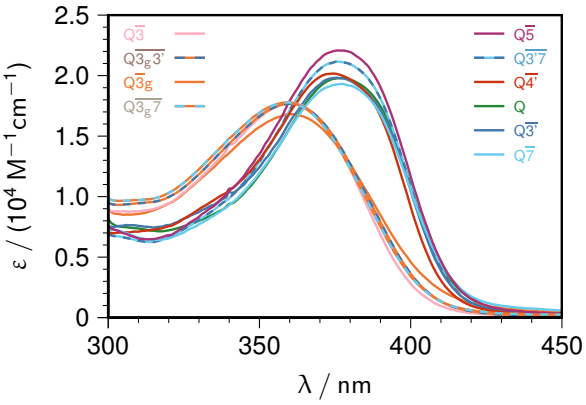

Supplementary Figure 11: Absorption spectra of all quercetin derivatives in their protonated forms (spectra invariant in an interval of at least 2 $\leq$ pH $\leq$ 6.5; upper limit for the 3-monosubstituted compounds, 6.2). Common conditions, 10 μM of substrate in 50 mM aqueous Triton TX-100 micellar solution. Compound / abbreviation: 3-O-methylquercetin / Q$\overline{3}$; narcissin Q$\overline{3_g3'}$; rutin / Q$\overline{3_g}$; rhamnetin-3-galactoside / Q$\overline{3_g7}$; azaleatin / Q$\overline{5}$; rhamnazin / Q$\overline{3'7}$; tamarixetin / Q$\overline{4'}$; quercetin / Q; isorhamnetin / Q$\overline{3'}$; rhamnetin / Q$\overline{7}$. For further explanation, see the text.

3 Radical Properties and Reactions

3.1 Photoionization Access

Supplementary Figure 12 sums up the relevant aspects of our method to generate the radicals $M^{\bullet}$ from our substrates MH. It uses an intense laser flash (355 nm, 5 ns, a few 100 mJ cm^{-2}) to achieve the conversion

$$MH \xrightarrow{h\nu} MH^{\bullet+} + e_{aq}^{\bullet-} \qquad \text{(S6)}$$

through photoionization. When the highly mobile and hydrophilic electron is ejected from MH inside a micelle, it will immediately relocalize to the surrounding aqueous bulk, which explains its formulation as hydrated electron $e_{aq}^{\bullet-}$ in Supplementary Equation S6.

For quercetin itself, it is known that the radical cation $MH^{\bullet+}$ is deprotonated quasi-instantaneously to give the desired neutral radical,[5]

$$MH^{\bullet+} \longrightarrow M^{\bullet} + H^{+} \qquad \text{(S7)}$$

and we expect the O-alkylated derivatives of quercetin to behave in the same way. The sequence of Supplementary Equations S6 and S7 thus yields equal amounts of $M^{\bullet}$ and $e_{aq}^{\bullet-}$, which can be used for calibrating the spectra of the neutral radical (or, when another deprotonation ensues, of the radical anion).

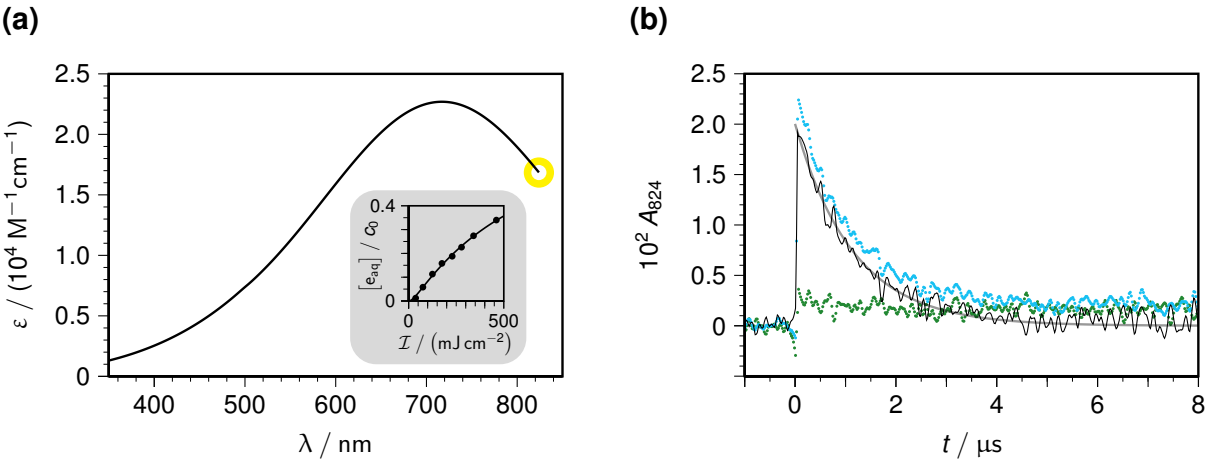

Supplementary Figure 12: Generation, characterization, and detection of the hydrated electron $e_{aq}^{\bullet-}$ through 355 nm laser photoionization of 10 µM (c_0) quercetin in 50 mM aqueous Triton TX-100 micellar solution. Graph (a): main plot, calibrated spectrum of $e_{aq}^{\bullet-}$ with the yellow circle indicating the chosen observation wavelength 824 nm; inset, relative $e_{aq}^{\bullet-}$ yield as function of the laser intensity $\mathcal{I}$ overlaid with fit curve of of biphotonic model, fit parameters without significance. Graph (b): dots, experimental absorption traces A_{824} at $\mathcal{I}$ = 461 mJ cm^{-2} in solution saturated with argon (cyan) and N_2O (green); thin line, difference of the two measurements, corresponding to the pure $e_{aq}^{\bullet-}$ absorption at 824 nm; thick curve, fit to a first-order decay. Experimental pH, 6.5. For further explanation, see the text.

This calibration is facilitated by the strong absorption of $e_{aq}^{\bullet-}$. The spectrum of $e_{aq}^{\bullet-}$ was measured independently by laser flash photolysis of water at 266 nm,[6] and calibrated by equating the maximum with the recently reported value of 22700 M^{-1}cm^{-1};[7] it is displayed in the main plot of Supplementary Figure 12a. We did not monitor $e_{aq}^{\bullet-}$ at the maximum but

at 824 nm, where our detection system exhibits a better sensitivity on account of a spike in the emission spectrum of our light source.

The absorptions of $e_{aq}^{\bullet-}$ and all other transients were separated by a simple procedure, which Supplementary Figure 12b illustrates. Its essence is a difference experiment that draws on Supplementary Equation S8,

$$e_{aq}^{\bullet-} + N_2O + H_2O \xrightarrow{h\nu} N_2 + HO^{\bullet} + HO^{-} \tag{S8}$$

N_2O is a specific scavenger of $e_{aq}^{\bullet-}$, and the reaction products are completely transparent in the visible and near-uv range. Carrying out the same photoionization experiment (i.e., with identical flash parameters) on the same solution twice, first under argon and then after saturation with N_2O, yields the absorption trace of all species except $e_{aq}^{\bullet-}$ (in the second run) and the pure $e_{aq}^{\bullet-}$ trace (as the point-by-point difference of both traces). Because the scavenging is diffusion controlled, the saturation concentration of N_2O in water suffices to complete the blanking out of $e_{aq}^{\bullet-}$ well within the duration of our laser pulse.[8]

We have already reported examples of the success of this procedure in micellar systems where it proved possible completely to eliminate "pathological" transient background effects near an insolubility limit.[8,9] It might be thought that a different secondary chemistry should result from the replacement of $e_{aq}^{\bullet-}$, which is a strongly reducing radical, by the strongly oxidizing $HO^{\bullet}$. However, our substrates are confined to the micelles; and $e_{aq}^{\bullet-}$, hence also $HO^{\bullet}$, are separated from them by the micelle–water interface. Consistent with this, we could not detect any such secondary chemistry in control experiments, for example, by comparing the kinetics in the difference spectrum with the kinetics under argon and the $e_{aq}^{\bullet-}$ absorption separated through the spectrum of Supplementary Figure 12a.

The dependence of the $e_{aq}^{\bullet-}$ yield on the laser intensity is explored in the inset of Supplementary Figure 12a. The apparent negative intercept indicates a biphotonic process.[6] No quantum yield can be extracted owing to the lack of a calibrated absorption spectrum of the S_1 excited state, but it is evident that up to 40 % of the substrate can be ionized by a single laser flash. The method is thus well suited as a radical generator in our systems.

As follows from Supplementary Equation S6, the substrate radicals should be formed in a concentration equal to $\left[e_{aq}^{\bullet-}\right]$, which allows a straightforward calibration of their extinction coefficients. If, however, the photoionization were accompanied by a direct photocleavage (i.e., homolysis) of phenolic O—H bonds as formulated in Supplementary Equation S9

$$MH \xrightarrow{h\nu} M^{\bullet} + H^{\bullet} \tag{S9}$$

this approach would give wrong results. Unfortunately, $H^{\bullet}$ is as transparent in our spectral observation range as is $HO^{\bullet}$; and control experiments by scavenging either $H^{\bullet}$ or the antioxidant-derived radicals proved infeasible in our micellar system, as opposed to homogeneous aqueous solution where we were able to establish the absence of the process of Supplementary Equation S9 for quercetin itself.[10] Based on the known fact that protic solvents strongly suppress phenolic homolyses,[11,12] we regard it as improbable that they

contribute to a significant degree in our systems on account of the TX-100 structure and the penetration of water into its micelles; but if that surmise were wrong, it would not falsify any of our results on the structures and kinetics of the radicals investigated herein.

In the example of Supplementary Figure 12b, the lifetime of $e_{aq}^{\bullet-}$ is slightly longer than 1 μs. With decreasing pH, the disappearance becomes faster because $e_{aq}^{\bullet-}$ is scavenged in a diffusion-controlled reaction with protons to give $H^{\bullet}$. By the same experiments as described above for $HO^{\bullet}$, we established that $H^{\bullet}$ does not cause any observable secondary chemistry in our systems. Down to approximately pH 3, the $e_{aq}^{\bullet-}$ decay is slow enough for the quantitative determination of its initial concentration with sufficient precision for calibrating the concentration of the antioxidant radicals.

In the pH range from 3 to 6.5, the $e_{aq}^{\bullet-}$ concentration remains constant at given laser energy, which facilitates comparisons. Evidently, the intermediate S_1 state absorbing the second (i.e., the ionizing) photon does not undergo a proton transfer that significantly changes its absorption spectrum at 355 nm. When the pH of the solution rises, the $e_{aq}^{\bullet-}$ yield invariably increases as the first pK_a is passed (compare, Supplementary Figures 2b–5b). It is to be expected that the photoionization of an anion is easier than that of a neutral molecule, but neither absolute nor relative quantum yields can be extracted from these experiments because the S_1 spectra are unavailable.

3.2 Radical Stabilities

The neutral radicals and radical anions slowly decay, as manifest from decreases of their absorbances towards about one-third (acidic solution) to one-half (neutral to basic solution) of the initial values (compare Supplementary Figure 13). The rate constant does not depend on pH and is $1.00 \times 10^3\ s^{-1}$ for quercetin. Considering that we recorded the transient spectra and investigated the deprotonations of the neutral radicals on a 50 times shorter timescale, the instability evidenced by Supplementary Figure 13 is negligible.

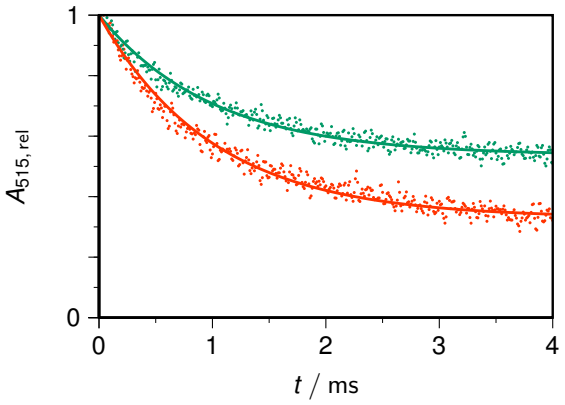

Supplementary Figure 13: Stabilities of the dominant neutral radicals (red, pH 3.0) and radical anions (green, pH 8.5) of quercetin in 50 mM TX-100 micelles. The normalized initial absorbances at 515 nm correspond to actual absorbances of about 10^{-2}, and the solid curves are global monoexponential fits with a lifetime of 1.00 ms. For further explanation, see the text.

3.3 Deprotonation Kinetics of NR3

Figure 14 displays combined pH and time dependences for NR3 deprotonation of the other substrates besides quercetin Q whose positions 3 and 4' are not blocked by substitution, namely, azaleatin Q$\overline{5}$ (14a), rhamnetin Q$\overline{7}$ (14b), rhamnazin Q$\overline{3'7}$ (14c), and isorhamnetin Q$\overline{3'}$ (14d).

For convenience, the fit functions given in the main article are repeated here as Equation S10 for the titration curves,

$$A_{\lambda,\infty,\mathrm{rel}} = \frac{A_{\lambda,\infty}}{A_{\lambda',\infty}} = \frac{\alpha}{1+10^{\mathrm{pH}-\mathrm{p}K_a}} + \frac{\beta}{1+10^{\mathrm{p}K_a-\mathrm{pH}}} \tag{S10}$$

and as Equation S11 for the kinetics.

$$A(t)_{\lambda,\mathrm{rel}} = A_{\lambda,\infty,\mathrm{rel}} + \frac{\alpha-\beta}{1+10^{\mathrm{p}K_a-\mathrm{pH}}} \times \exp\left[-k_{\mathrm{dep}}\left(1+10^{\mathrm{p}K_a-\mathrm{pH}}\right)t\right] \tag{S11}$$

For Figure 14, λ and λ' are 580 and 515 nm.

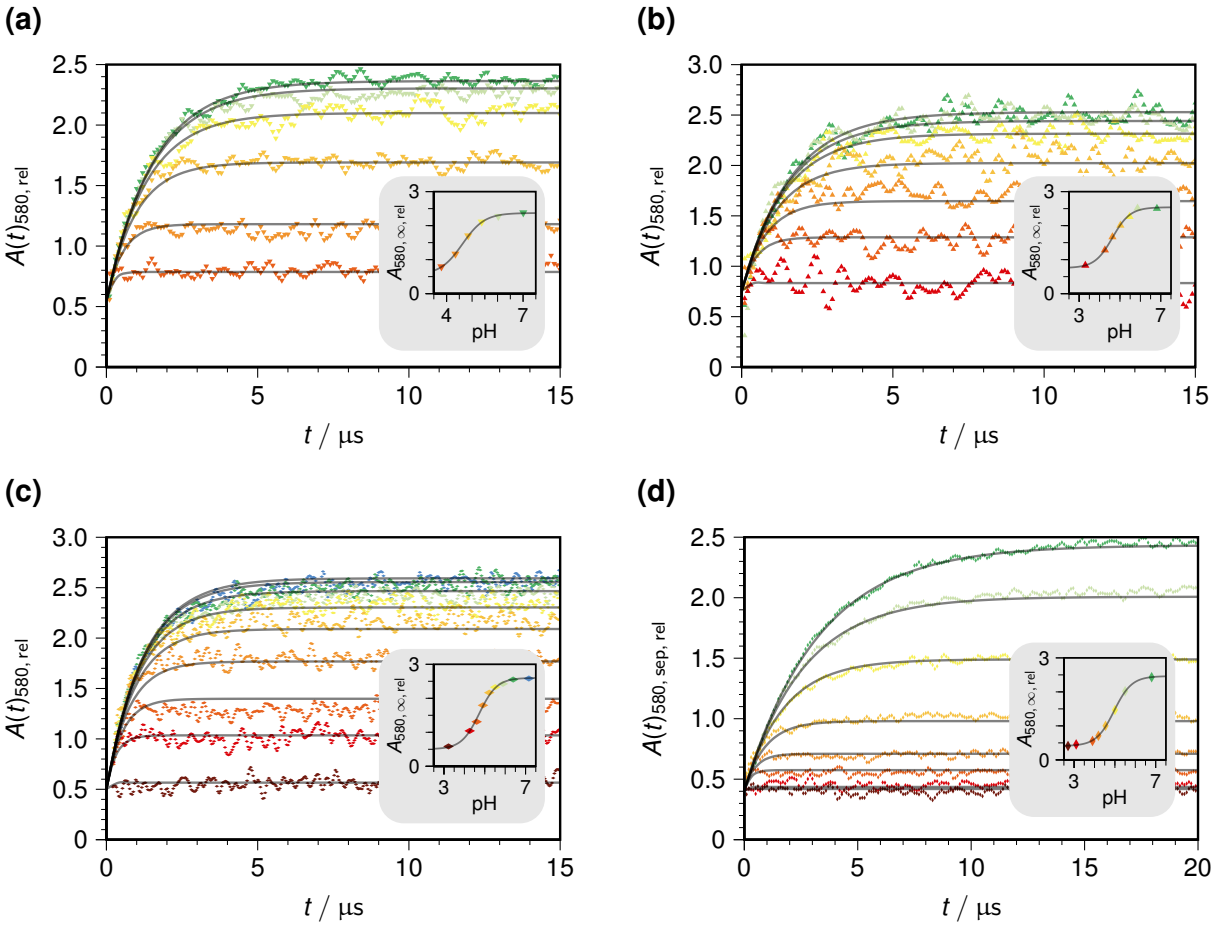

Supplementary Figure 14: Deprotonation of the neutral radicals NR3 to give the radical anions RAN34'. Graph (a), azaleatin Q$\overline{5}$; graph (b), rhamnetin Q$\overline{7}$; graph (c), rhamnazin Q$\overline{3'7}$; graph (d), isorhamnetin Q$\overline{3'}$. Insets, titration curves of the end values $A_{580,\infty,\mathrm{rel}}$ at 580 nm relative to those at 515 nm; main plots, traces $A(t)_{580,\mathrm{rel}}$ relative to the same reference, each with the same color code as in the pertaining inset. Best fit pK_a (Equation S10) and rate constant k_{dep} (Equation S11): (a), 4.62 and 6.4 $\times$ 10^5 s^{-1}; (b), 4.63 and 6.2 $\times$ 10^5 s^{-1}; (c), 4.73 and 8.1 $\times$ 10^5 s^{-1}; (d), 4.95 and 3.0 $\times$ 10^5 s^{-1}. For further explanation, see the text.

4 Quantum-Mechanical Calculations

We used the Gaussian 16 program[13] for all our DFT calculations. Unless noted otherwise, the level of theory was (U)B3LYP/6-311++g(2d,2p) and all computations were performed in the solvent MeOH with the IEFPCM model. After geometry optimization, frequencies were calculated; if the analytical gradients used in the latter step indicated that a stationary point was narrowly missed, the cycle was repeated. Lastly, TDDFT (15 states) computations on the stationary points yielded the transition wavelengths λ_i and oscillator strengths p_i.

It is convenient to convert wavelengths λ to wavenumbers $\tilde{\lambda}$ with Supplementary Equation S12,

$$\tilde{\lambda}\left[\text{in cm}^{-1}\right] \quad = \quad \frac{10^7}{\lambda\,[\text{in nm}]} \tag{S12}$$

The formula (Supplementary Equation S13) to obtain the spectra $\varepsilon(\tilde{\lambda})$ from the list of $\left(\tilde{\lambda}_i, p_i\right)$ contains a width parameter $\tilde{\sigma}$ and a shift parameter $\tilde{s}$, both in units of cm^{-1}. For a given radical, we kept $\tilde{\sigma}$ and $\tilde{s}$ constant.

$$\varepsilon(\tilde{\lambda})\left[\text{in M}^{-1}\text{cm}^{-1}\right] \quad = \quad \frac{1.3063 \times 10^8}{\tilde{\sigma}} \sum_i p_i \exp\left[-\left(\frac{\tilde{\lambda}-\tilde{s}-\tilde{\lambda}_i}{\tilde{\sigma}}\right)^2\right] \tag{S13}$$

All spectra of Supplementary Figure 15–16 were calculated with $\tilde{\sigma}$ equal to 3226 cm^{-1} (0.4 eV, i.e., the default value of Gaussian 16).

4.1 Energy Comparisons between Gaussian 03 and Gaussian 16

Gaussian 03 calculations on the neutral radicals NR*x* of quercetin in water gave a stability order NR3 $<$ NR4' $<$ NR3' $<$ NR7 $<$ NR5, with Gibbs free energies relative to NR3 being 1.2, 3.0, 11.0 and 11.2 kcal/mol.[5] However, when we repeated these calculations with Gaussian 16 using exactly the same geometry (which was fully specified in the original publication), quantum-mechanical model and basis set (B3LYP/6-311+g(d,p)), thermochemical scaling factor (0.9806) and solvent model (PCM), we obtained a stability order with NR3 and NR4' interchanged and deviations between our Gaussian 16 and the reported Gaussian 03 Gibbs free energies that were substantial for NR3 (+2.9 kcal/mol) and NR5 (+4.4 kcal/mol). This Section summarizes our attempts to find the reason.

Supplementary Table 1 first compares the electronic energies EE(vacuum) to ensure the absence of misprints in the published[5] geometries. The very small discrepancies of 0.01 ± 0.02 kcal/mol rule out this source of errors.

Next, Supplementary Table 2 juxtaposes the results on the thermal corrections C_T to the Gibbs free energies. There are differences, which we ascribe to two factors. First, the Gaussian 03 calculations apparently used the correction for the frequencies in vacuum

Supplementary Table 1: Comparison between electronic energies EE in vacuum calculated for quercetin radicals with Gaussian 16 and reported for Gaussian 03[5]

Radical	Gaussian 03[a] EE(vacuum) in Ha	Gaussian 16 EE(vacuum) in Ha	Comparison Δ[b] in kcal/mol
NR3	−1103.872719	−1103.872738	−0.01
NR3'	[c]	−1103.882151	n/a
NR4'	−1103.8861223	−1103.886143	−0.01
NR5	−1103.8505164	−1103.850473	0.03
NR7	−1103.8638607	−1103.863829	0.02

[a] Values from the Supporting Information of Ref 5 [b] Difference between the values computed with Gaussian 16 and reported for Gaussian 03[5] [c] Value not specified

also for the solution. Second, the calculations were not really done at a stationary point because the geometry optimization was apparently performed at a slightly lower level than the frequency analysis and PCM calculation, 6-31+g(d,p) instead of 6-311+g(d,p). Despite these problems, differences C_T cannot account for the stability inversion of NR3 and NR4' although they favour the latter over the former by about 0.3 kcal/mol.

Supplementary Table 2: Comparison between thermal corrections to Gibbs Free Energy C_T calculated for quercetin radicals with Gaussian 16 and reported for Gaussian 03[5]

Radical	Gaussian 03[a]	Gaussian 16		Comparisons	
	C_T(vacuum) in Ha	C_T(vacuum) in Ha	C_T(water) in Ha	Δ_1[b] in kcal/mol	Δ_1[c] in kcal/mol
NR3	0.165424	0.165572	0.163998	0.09	−0.89
NR3'	0.166151	0.167132	0.166004	0.62	−0.09
NR4'	0.167690	0.167060	0.165835	−0.40	−1.16
NR5	0.164050	0.164430	0.163426	0.24	−0.39
NR7	0.165045	0.165293	0.163102	0.16	−1.22

[a] Values from the Supporting Information of Ref 5 [b] Difference between the values in vacuum computed with Gaussian 16 and reported for Gaussian 03[5] [c] Difference between the values computed with Gaussian 16 in water and reported for Gaussian 03 in vacuum only[5]

This leaves the electronic energy EE(water) as the explanation for the discrepancy in the stability order. Because of the absence (see Supplementary Table 1 above) of a version effect on EE(vacuum), this pinpoints changes in the implementation and/or parametrization

of the PCM model that were introduced in Gaussian 09 (and retained, possibly modified again, in Gaussian 16) as the underlying reason. Supplementary Table 3 provides numerical corroboration. It is evident that the differential rise in EE(water) by 2.9 kcal/mol between NR3 and NR4' is more than twice as large than the stability difference calculated by Gaussian 03, leading to the observed inversion.

Supplementary Table 3: Comparison between electronic energies EE in water calculated for quercetin radicals with Gaussian 16 and and reported for Gaussian 03 [5]

Radical	Gaussian 03[a] EE(water)[b] in Ha	Gaussian 16 EE(water) in Ha	Comparison Δ[c] in kcal/mol
NR3	−1103.902902	−1103.896811	3.82
NR3'	−1103.898842	−1103.897472	0.86
NR4'	−1103.903187	−1103.901760	0.90
NR5	−1103.883714	−1103.876146	4.75
NR7	−1103.884922	−1103.882595	1.46

[a] Values from the Supporting Information of Ref 5 [b] Specified as "total free energy in solution: with all non-electrostatic terms" in Ref 5 [c] Difference between the values computed with Gaussian 16 and reported for Gaussian 03 [5]

We further checked whether the old Gaussian 03 results can be obtained by using Gaussian 16 in compatibility mode (keyword "G03defaults"; this also necessitates numerical second derivatives instead of analytical ones, keyword "Freq=Numer"). Supplementary Table 4 collects the results for the procedure of Ref 5. As is evident, the values for EE(water) displays a nearly constant offset of -10.80 ± 0.09 kcal/mol relative to the old ones, which indicates some change of the SCRF parameters even in compatibility mode. However, a constant offset plays no role when energy differences between radicals are considered; and on the basis of EE(water) alone, it would thus clearly be possible to reproduce the old energy order. That this does not work at the fixed geometry is solely due to C_T, which exhibits differences large enough to change the energetic ordering such that NR4' becomes lowest again.

Because according to the Gaussian manual "... it is meaningless to compute frequencies at any geometry other than a stationary point for the method used ... For example, computing 6-311G(d) frequencies at a 6-31G(d) optimized geometry produces meaningless results",[13] we lastly reoptimized the geometries specified in Ref 5 with Gaussian 16 in Gaussian 03 compatibility mode and carried out the remainder of these calculations in the same mode. We restricted these comparisons to the three most important radicals NR3, NR3', and NR4'. As can be seen in Supplementary Table 5, this approach led to a near-constant decrease of EE(water) by as much as 1.2 kcal/mol but — in accordance

Supplementary Table 4: Comparisons between thermal corrections to Gibbs Free Energy C_T and electronic energy EE in water calculated for quercetin radicals with Gaussian 16 in compatibility mode (G03defaults) at the fixed geometry specified in Ref 5 and reported for Gaussian 03 [5]

	Gaussian 16 compatibility mode		Comparisons		
Radical	C_T(water) in Ha	EE(water) in Ha	$\Delta_1^{[a]}$ in kcal/mol	$\Delta_1^{[b]}$ in kcal/mol	$\Delta_1^{[c]}$ in kcal/mol
NR3	0.163898	−1103.920160	−0.96	−10.83	1.33
NR3'	0.163591	−1103.915994	−1.61	−10.76	3.76
NR4'	0.161946	−1103.920335	−3.60	−10.76	(0)
NR5	0.159952	−1103.901069	−2.57	−10.89	10.84
NR7	0.162124	−1103.902076	−1.83	−10.76	11.57

[a] Differences between the second column of this Table and the second column of Supplementary Table 2 (values from the Supporting Information of Ref 5) [b] Differences between the third column of this Table and the second column of Supplementary Table 3 (values from the Supporting Information of Ref 5) [c] Sums of the values in the second and third columns of this Table relative to their minimum value

with expectation based on the above passage from the manual — to changes in C_T that amounted to more than just a constant offset, such that the reported stability order was obtained, albeit with differences in ΔG of typically ± 0.6 kcal/mol.

Supplementary Table 5: Comparisons between thermal corrections to Gibbs Free Energy C_T and electronic energy EE in water calculated for quercetin radicals with Gaussian 16 in compatibility mode (G03defaults) after reoptimizing the geometry specified in Ref 5 and reported for Gaussian 03 [5]

	Gaussian 16 compatibility mode		Comparisons		
Radical	C_T(water) in Ha	EE(water) in Ha	$\Delta_1^{[a]}$ in kcal/mol	$\Delta_1^{[b]}$ in kcal/mol	$\Delta_1^{[c]}$ in kcal/mol
NR3	0.162332	−1103.921940	−1.94	−11.95	(0)
NR3'	0.163983	−1103.918036	−1.36	−12.04	3.49
NR4'	0.163519	−1103.922316	−2.62	−12.00	0.51

[a] Differences between the second column of this Table and the second column of Supplementary Table 2 (values from the Supporting Information of Ref 5) [b] Differences between the third column of this Table and the second column of Supplementary Table 3 (values from the Supporting Information of Ref 5) [c] Sums of the values in the second and third columns of this Table relative to their minimum value

Because the SCRF convergence rate of Gaussian 16 appears to be so much faster than that of Gaussian 03 was, the questions of whether a change of basis set is necessary or whether C_T needs to be calculated in vacuum instead of in the medium are no longer important for molecules of this size. The changes of EE(water) in Supplementary Table 4 are clear indications of a reparametrization of the SCRF model; but it is not believable that a newer program version would produce worse results with respect to one of its key output

elements (the electronic energy) than the more than ten years older antepenultimate version. On these grounds, we surmise that the ”better” results of the older version are not caused by that version being better but by accidental error compensations in it.

4.2 Separating the Energy Contributions

In detail, the numbers for the separation discussion in the main article are the following. The Gibbs free energies are specified relative to the reference points in Figure 2b of the main article. Comparisons are only made between near-identical conjugated systems, and all errors are r.m.s. errors.

4.2.1 Intrinsic electronic difference between NR3’ and NR4’

- Quercetin Q

  ΔG° (NR3’), 2.0 kcal/mol; ΔG° (NR4’), 0.0 kcal/mol

  Difference, 2.0 kcal/mol; all hydrogen bonds intact
- Rhamnetin Q$\overline{7}$

  ΔG° (NR3’), 2.9 kcal/mol; ΔG° (NR4’), 0.0 kcal/mol

  Difference, 2.9 kcal/mol; all hydrogen bonds intact
- Tamarixetin Q$\overline{4'}$ and Isorhamnetin Q$\overline{3'}$
  - Q$\overline{4'}$: ΔG° (NR7), 7.9 kcal/mol; ΔG° (NR3’), 3.5 kcal/mol

    Difference, 4.4 kcal/mol; catechol hydrogen bond missing, all others intact
  - Q$\overline{3'}$: ΔG° (NR7), 8.1 kcal/mol; ΔG° (NR4’), 1.1 kcal/mol

    Difference, 7.0 kcal/mol; catechol hydrogen bond missing, all others intact

  For this pair, NR3’ is thus less stable than NR4’ by 2.6 kcal/mol.

Averaging the three cases gives a stability difference of 2.5 ± 0.4 kcal/mol.

4.2.2 Catechol hydrogen bond in NR*x*

- Quercetin Q and isorhamnetin Q$\overline{3'}$
  - Q: ΔG° (NR7), 11.1 kcal/mol; ΔG° (NR4’), 0.0 kcal/mol

    Difference, 11.1 kcal/mol; all hydrogen bonds intact
  - Q$\overline{3'}$: ΔG° (NR7), 8.1 kcal/mol; ΔG° (NR4’), 1.1 kcal/mol

    Difference, 7.0 kcal/mol; catechol hydrogen bond missing, all others intact

  For this pair, NR4’ without the catechol bond is thus less stable by 4.1 kcal/mol.
- 3-O-methylquercetin Q$\overline{3}$ and 3,3’-di-O-methylquercetin Q$\overline{33'}$
  - Q$\overline{3}$: ΔG° (NR7), 11.2 kcal/mol; ΔG° (NR4’), 0.0 kcal/mol

    Difference, 11.2 kcal/mol; all hydrogen bonds except $O^3H\cdots O{=}C$ intact
  - Q$\overline{33'}$: ΔG° (NR7), 6.7 kcal/mol; ΔG° (NR4’), 0.0 kcal/mol

Difference, 6.7 kcal/mol; catechol hydrogen bond and $O^3H\cdots O{=}C$ missing, $O^5H\cdots O{=}C$ intact

For this pair, NR4' without the catechol bond is thus less stable by 4.5 kcal/mol.

- Quercetin Q and tamarixetin Q$\overline{4'}$
  - Q: ΔG° (NR7), 11.1 kcal/mol; ΔG° (NR3'), 2.0 kcal/mol

    Difference, 9.1 kcal/mol; all hydrogen bonds intact
  - Q$\overline{4'}$: ΔG° (NR7), 7.9 kcal/mol; ΔG° (NR3'), 3.5 kcal/mol

    Difference, 4.4 kcal/mol; catechol hydrogen bond missing, all others intact

  For this pair, NR3' without the catechol bond is thus less stable by 4.7 kcal/mol.

Averaging the three cases gives a stability difference of 4.4 $\pm$ 0.3 kcal/mol.

4.2.3 Hydrogen bond between O^5H and carbonyl in NR*x*

- Quercetin Q

  ΔG° (NR5), 14.2 kcal/mol; ΔG° (NR7), 11.1 kcal/mol

  Difference, 3.1 kcal/mol; no change of hydrogen bonds other than for $O^5H\cdots O{=}C$
- Isorhamnetin Q$\overline{3'}$

  ΔG° (NR5), 11.6 kcal/mol; ΔG° (NR7), 8.1 kcal/mol

  Difference, 3.5 kcal/mol; no change of hydrogen bonds other than for $O^5H\cdots O{=}C$
- Tamarixetin Q$\overline{4'}$

  ΔG° (NR5), 11.7 kcal/mol; ΔG° (NR7), 7.9 kcal/mol

  Difference, 3.8 kcal/mol; no change of hydrogen bonds other than for $O^5H\cdots O{=}C$

Averaging the three cases gives a stability difference of 3.5 $\pm$ 0.3 kcal/mol.

4.2.4 NR3 (compounded energy)

- Quercetin Q

  ΔG° (NR7), 11.1 kcal/mol; ΔG° (NR3), 2.5 kcal/mol

  Difference, 8.6 kcal/mol; no change of hydrogen bonds other than for $O^3H\cdots O{=}C$
- Isorhamnetin Q$\overline{3'}$

  ΔG° (NR7), 8.1 kcal/mol; ΔG° (NR3), 0.0 kcal/mol

  Difference, 8.1 kcal/mol; no change of hydrogen bonds other than for $O^3H\cdots O{=}C$
- Tamarixetin Q$\overline{4'}$

  ΔG° (NR7), 7.9 kcal/mol; ΔG° (NR3), 0.0 kcal/mol

  Difference, 7.9 kcal/mol; no change of hydrogen bonds other than for $O^3H\cdots O{=}C$

Averaging the three cases gives a stability difference of 8.2 $\pm$ 0.3 kcal/mol. The gain by the electronically more stable radical NR3 is partly offset by the unavoidable loss of the

hydrogen bond between O^3H and the carbonyl oxygen.

4.2.5 Catechol hydrogen bond in RAN*xy*

- Quercetin Q and isorhamnetin Q$\overline{3'}$
  - Q: ΔG° (RAN37), 6.4 kcal/mol; ΔG° (RAN34'), 0.0 kcal/mol
    Difference, 6.4 kcal/mol; all hydrogen bonds intact
  - Q$\overline{3'}$: ΔG° (RAN37), 0.0 kcal/mol; ΔG° (RAN34'), 0.6 kcal/mol
    Difference, -0.6 kcal/mol; catechol hydrogen bond lost, all others intact

  For this pair, the loss of the catechol bond costs 7.0 kcal/mol.
- Quercetin Q and tamarixetin Q$\overline{4'}$
  - Q: ΔG° (RAN37), 6.4 kcal/mol; ΔG° (RAN33'), 6.6 kcal/mol
    Difference, -0.2 kcal/mol; all hydrogen bonds intact
  - Q$\overline{4'}$: ΔG° (RAN37), 0.0 kcal/mol; ΔG° (RAN33'), 7.2 kcal/mol
    Difference, -7.2 kcal/mol; catechol hydrogen bond lost, all others intact

  For this pair, the loss of the catechol bond costs 7.0 kcal/mol.

The two cases gives exactly the same energy contribution of 7.0 kcal/mol.

4.2.6 Intrinsic electronic difference between RAN33' and RAN34'

- With catechol hydrogen bond remaining intact
  For quercetin Q and rhamnetin Q$\overline{7}$, RAN33' is higher in energy than RAN34' by 6.6 and 6.5 kcal/mol.
- With catechol hydrogen bond lost
  From the data in Section 4.2.5, RAN33' of tamarixetin Q$\overline{4'}$ lies 7.2 kcal/mol above RAN37, and RAN34' of isorhamnetin Q$\overline{3'}$ lies 0.6 kcal/mol below RAN37. The difference is 7.8 kcal/mol.

Averaging the three cases gives 7.0 $\pm$ 0.6 kcal/mol. We have excluded azaleatin Q$\overline{5}$ from this analysis because of the missing hydrogen bond to the end atom of the conjugated system, as opposed to the other three compounds.

4.2.7 Intrinsic electronic difference between RAN3'4' and RAN34'

For quercetin Q, azaleatin Q$\overline{5}$, and Rhamnetin Q$\overline{7}$, where RAN34' as the lowest-energy radical anion always constitutes the reference point, the difference is 4.9, 5.2, and 4.7 kcal/mol. The average is thus 4.9 $\pm$ 0.2 kcal/mol.

4.3 Calculated Spectra of the Radical Cations and Neutral Radicals

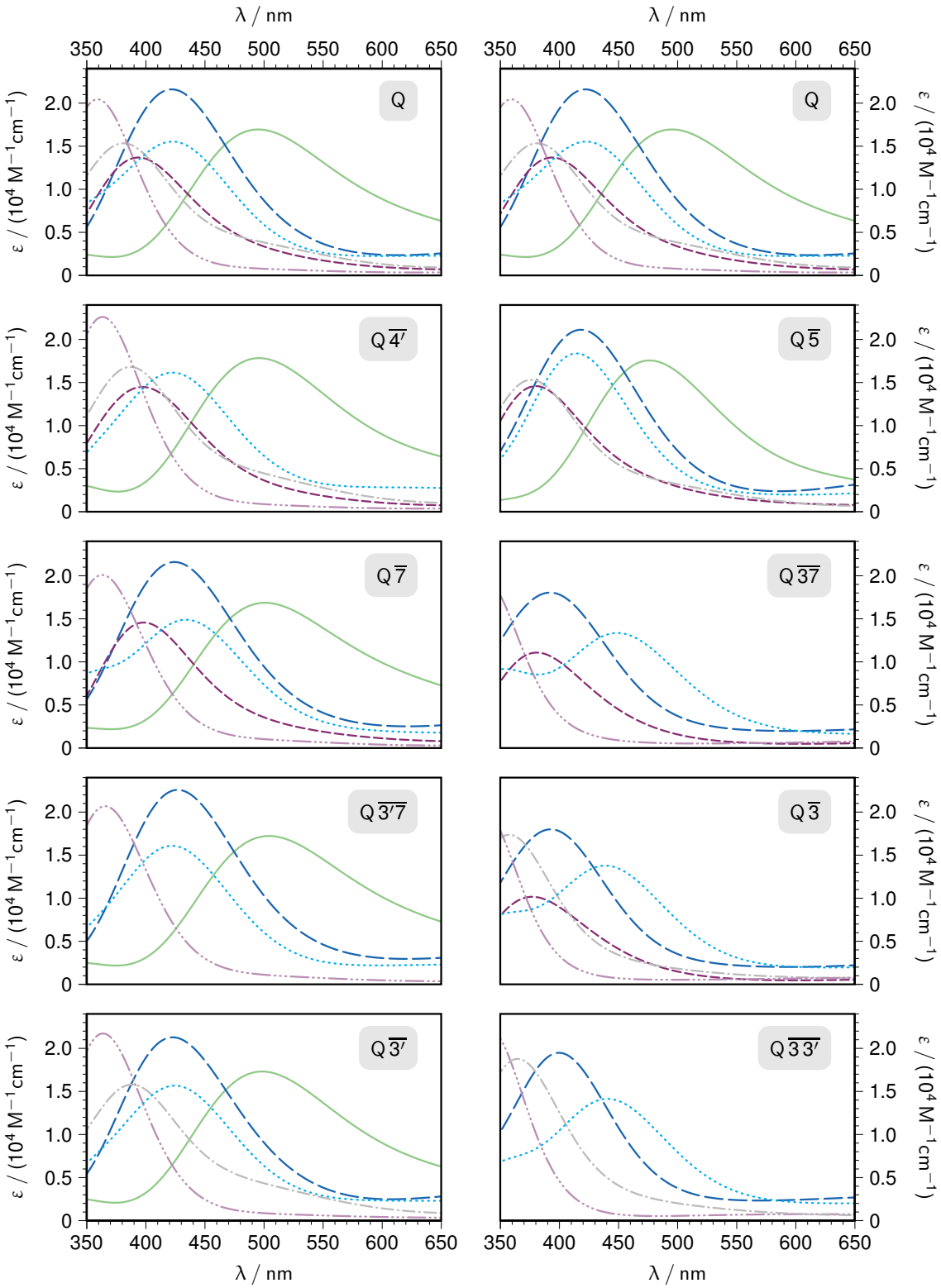

Supplementary Figure 15: Calculated absorption spectra (TDDFT, B3LYP/6-311++G(2d,2p), IEFPCM, solvent MeOH) of the neutral radicals NR*x* and radical cations RC of quercetin and O-alkylated derivatives thereof. Substrate abbreviation as in Supplementary Figure 11. Line type and color code: NR3, solid, green ; NR4', long dashed, blue; NR3', short dashed, violet; NR7, dot-dash, gray; NR5, dot-dot-dot-dash, pale violet; RC, dotted, cyan. For further explanation, see the text.

4.4 Calculated Spectra of the Radical Anions

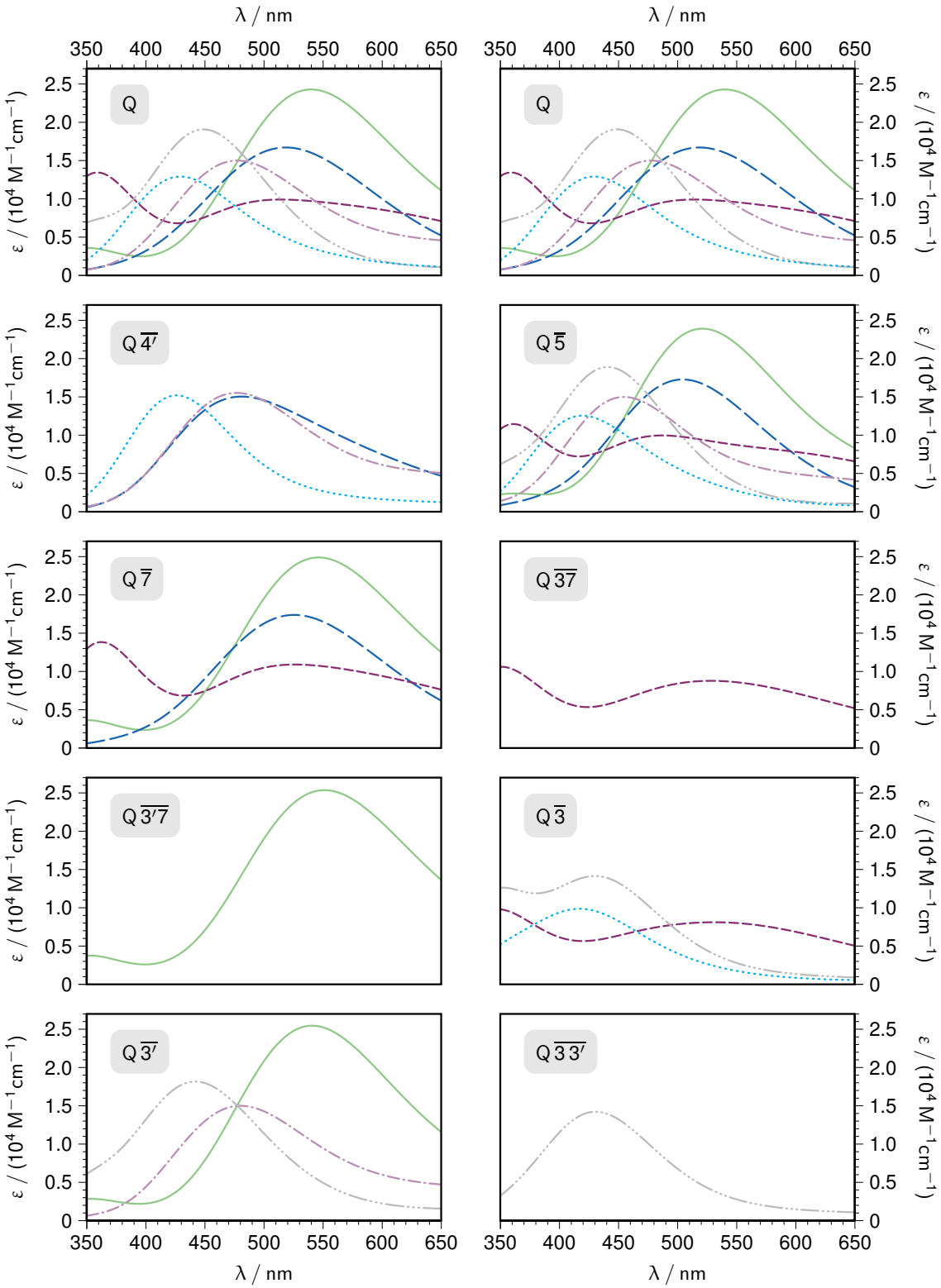

Supplementary Figure 16: Calculated absorption spectra (TDDFT, B3LYP/6-311++G(2d,2p), IEFPCM, solvent MeOH) of the radical anions RAN*xy* of quercetin and O-alkylated derivatives thereof. Substrate abbreviation as in Supplementary Figure 11. Line type and color code: RAN34', solid, green ; RAN33', long dashed, blue; RAN3'4', short dashed, violet; RAN37, dot-dash, pale violet; RAN4'7, dot-dot-dot-dash, gray; RAN3'7, dotted, cyan. For further explanation, see the text.

Supplementary References

[1] M. Goez, C. Kerzig and R. Naumann, *Angew. Chem. Int. Ed.*, 2014, **53**, 9914–9916.

[2] T. Morisue, Y. Moroi and O. Shibata, *J. Phys. Chem.*, 1994, **98**, 12995–13000.

[3] F. H. Quina, P. M. Nassar, J. B. S. Bonilha and B. L. Bales, *J. Phys. Chem.*, 1995, **99**, 17028–17031.

[4] S. K. Hait and S. P. Moulik, *J. Surfactants Deterg.*, 2001, **4**, 303–309.

[5] R. Amorati, A. Baschieri, A. Cowden and L. Valgimigli, *Biomimetics*, 2017, **2**, 9–21.

[6] C. Kerzig and M. Goez, *Phys. Chem. Chem. Phys.*, 2015, **17**, 13829–13836.

[7] P. M. Hare, E. A. Price and D. M. Bartels, *J. Phys. Chem. A*, 2008, **112**, 6800–6802.

[8] T. Kohlmann, R. Naumann, C. Kerzig and M. Goez, *Photochem. Photobiol. Sci.*, 2017, **16**, 185–192.

[9] M. Goez, D. von Ramin-Marro, M. Schiewek and M. H. O. Musa, *Z. Phys. Chem. (Muenchen, Ger.)*, 2014, **228**, 193–207.

[10] T. Kohlmann and M. Goez, *Chem. Eur. J.*, 2020, **26**, 17428–17436.

[11] J.-C. Mialocq, J. Sutton and P. Goujon, *J. Chem. Phys.*, 1980, **72**, 6338–6345.

[12] C. Grieco, A. T. Hanes, L. Blancafort and B. Kohler, *J. Phys. Chem. A*, 2019, **123**, 5356–5366.

[13] M. J. Frisch, G. W. Trucks, H. B. Schlegel, G. E. Scuseria, M. A. Robb, J. R. Cheeseman, G. Scalmani, V. Barone, G. A. Petersson, H. Nakatsuji, X. Li, M. Caricato, A. V. Marenich, J. Bloino, B. G. Janesko, R. Gomperts, B. Mennucci, H. P. Hratchian, J. V. Ortiz, A. F. Izmaylov, J. L. Sonnenberg, D. Williams-Young, F. Ding, F. Lipparini, F. Egidi, J. Goings, B. Peng, A. Petrone, T. Henderson, D. Ranasinghe, V. G. Zakrzewski, J. Gao, N. Rega, G. Zheng, W. Liang, M. Hada, M. Ehara, K. Toyota, R. Fukuda, J. Hasegawa, M. Ishida, T. Nakajima, Y. Honda, O. Kitao, H. Nakai, T. Vreven, K. Throssell, J. A. Montgomery, Jr., J. E. Peralta, F. Ogliaro, M. J. Bearpark, J. J. Heyd, E. N. Brothers, K. N. Kudin, V. N. Staroverov, T. A. Keith, R. Kobayashi, J. Normand, K. Raghavachari, A. P. Rendell, J. C. Burant, S. S. Iyengar, J. Tomasi, M. Cossi, J. M. Millam, M. Klene, C. Adamo, R. Cammi, J. W. Ochterski, R. L. Martin, K. Morokuma, O. Farkas, J. B. Foresman and D. J. Fox, *Gaussian 16 Revision C.01*, 2016, Gaussian Inc. Wallingford CT.